Rheology of crystal-bearing natural magmas: Torsional deformation experiments at 800°C and 100MPa

Satoshi Okumura, Alexandra Roma Larisa Kushnir, Caroline Martel, Rémi Champallier, Quentin Thibault, Shingo Takeuchi

Rheology of crystal-bearing natural magmas: Torsional deformation experiments at 800 °C and 100 MPa

Satoshi Okumura , Alexandra R.L. Kushnir, Caroline Martel, Rémi Champallier, Quentin Thibault, Shingo Takeuchi

Highlights

- Natural magma shows rheology similar to synthetic magmas at a 16 vol% crystallinity.
- A strong dependence on strain rate was observed in magma with a 45 vol% crystallinity.

Abstract

Rheological behavior of crystal-bearing magma is a controlling factor of magma flow dynamics and hence the style of volcanic eruptions. In this study, we performed torsional deformation experiments to determine the viscosity of crystal-bearing rhyolitic and dacitic magmas. The experiments were conducted at a temperature of 800 °C and under confining and pore fluid pressures of 100 and 80 MPa, respectively, by using an internally heated gas-medium deformation apparatus. To simulate the rheology of natural magma, we deformed volcanic rocks with 16 and 45 vol% crystallinities and < 4 vol% gas bubbles. These rocks have different crystal and bubble shape and size, which appear to influence magma rheology. By using the mechanical data obtained, we calculated flow indices and viscosities for these magmas. For magma with 16 vol% crystallinity, the flow index showed good agreement with previous data obtained from experiments on synthetic magma analogues and model predictions. In contrast, the flow index was smaller than those obtained from previous experiments and model predictions at 45 vol% crystallinity, which may be explained by considering that natural magma contains crystals with different shapes and sizes. We also found that the apparent viscosity of the magma increased when sample-scale fractures were observed in run products. This means that the heterogeneity of natural magma causes locally stiff regions within the sample owing to crystal interaction.

Our data indicate that the viscosity of crystal-rich magma is strongly dependent on the strain rate. This implies that magma ascending in a volcanic conduit shows a plug-type flow because the viscosity decreases near the conduit rim where the strain rate is high. Additionally, if shear localises near the rim, a currently unrecognised mechanism may contribute to outgassing from the central portion of the conduit because outgassing is difficult to facilitate without shear deformation.

Keywords : Magma rheology; Bubble- and crystal-bearing magma; High PT deformation experiment

1. Introduction

Knowledge of magma rheology is fundamental to understanding and modelling volcanic eruptions, because it controls the initiation of magma ascent (eruptibility) (e.g., Marsh, 1981, Scaillet et al., 1998 and Takeuchi, 2004), the dynamics of conduit flow (e.g., Melnik and Sparks, 1999 and Kozono and Koyaguchi, 2012), and the eruption style to the surface through fragmentation (e.g., Papale, 1999, Zhang, 1999a and Zhang, 1999b). Numerous experimental studies have been performed to investigate magma rheology, particularly to determine the viscosity of crystal- and bubble-bearing magmas (e.g., Lejeune and Richet, 1995 and Manga et al., 1998; and references in Mader et al., 2013). The effect of crystals on magma viscosity has been well-researched in previous studies, which have shown that magma viscosity increases rapidly near a critical crystallinity (α_{crit}) and that the critical value is controlled by crystal shape (e.g., Lejeune and Richet, 1995, Caricchi et al., 2007, Mueller et al., 2011 and Picard et al., 2013). The crystal-bearing magmas also show shear thinning behavior when the crystallinity approaches α_{crit}. A model for the viscosity of bubble-bearing magma has been proposed on the basis of experimental data (e.g., Pal, 2003 and Llewellin and Manga, 2005). The viscosity of bubble-bearing magma is lower than that of bubble-free magma when the capillary number (Ca) is larger than a critical Ca (Ca_{crit}), whereas it is higher at $Ca < Ca_{crit}$ (Pal, 2003). It has also been proposed that the dynamic capillary number should be considered when characterising the rheology of bubble-bearing magma under unsteady flow (Llewellin et al., 2002).

As a next step to understanding the rheology of actual magma, we need to consider the effect of different sizes and shapes of crystals and the combined effects of both crystals and bubbles. Recent analogue experiments have demonstrated that crystals with different sizes and shapes strongly influence magma rheology (e.g., Cimarelli et al.,

Moitra and Gonnermann, 2015). These studies largely contribute to the understanding of theoretical aspect for the effects of different crystal sizes and shapes on magma rheology; we need to test the results obtained by these studies for natural magmas (Lavallée et al., 2007; Caricchi et al., 2008; Avard and Whittington, 2012; Vona et al., 2013). Recent experiments with analogue materials and synthetic magmas also focus on the combined effects of crystals and bubbles (e.g., Pistone et al., 2012; Truby et al., 2015). In analogue experiments using glass beads and sugar syrup, experimental data were well reproduced by a model in which the bubble-bearing liquid is a continuous ("effective") medium that suspends solid particles under steady-flow conditions (Truby et al., 2015). High-temperature and high-pressure experiments on synthetic magmatic analogues also showed that viscosity commonly decreases by adding bubbles. At crystallinities <~50 vol%, this result can be roughly understood by a model in which the effects of crystals and bubbles are included (Shields et al., 2014). In contrast, the complicated rheology of crystal-rich magma, i.e. both strain hardening and weakening, was observed in experiments performed under the same experimental condition, although relatively homogeneous synthesised materials were used (Pistone et al., 2013).

Experiments using homogeneous analogue materials provide a basic understanding of magma rheology. However, actual magmas are heterogeneous in terms of size, number, shape, and the spatial distribution of crystals and bubbles; it is difficult to simulate magma perfectly using analogue materials. In this study, we investigate the rheology of natural magmas which includes crystals and bubbles of different size and shape, by using volcanic rock samples as starting materials.

2. Experimental and analytical methods

2.1. Starting materials

We selected two volcanic rocks with different crystal contents of 16 and 45 vol% to investigate magma rheology. These samples are lava from Mukaiyama volcano, Niijima, Japan (referred to as MY in this study) and pumice from the Ootagirigawa pyroclastic flow, Myoko volcano, Japan (MO). The major phenocryst phases are quartz and plagioclase for MY and plagioclase, orthopyroxene, and hornblende for MO (Fig. 1) (Isshiki, 1987; Hasenaka et al., 1995). The MY sample also contains trace amounts of biotite. The groundmass of MY is glassy (Fig. 1a and c), whereas plagioclase and pyroxene microlites formed in the groundmass of MO (Fig. 1b and d).

The bulk rock compositions determined by X-ray fluorescence (XRF) are rhyolite and dacite for the lava (MY) and pumice (MO), respectively. The chemical composition of matrix glasses, measured by electron probe microanalyser, is rhyolite for both samples (Table 1). Total volume fractions of crystals (crystallinities) were estimated based on mass balance of K_2O content for bulk and glass compositions; hence, they represent the sum of both phenocrysts and microlites. For mass balance calculation, we assumed the densities of 2300 and 2700 kg m^{-3} for rhyolitic glass and crystal of MY, respectively, and 2300 and 2900 kg m^{-3} for rhyolitic glass and crystal of MO, respectively, based on major phenocryst phases, i.e., quartz and plagioclase in MY, and plagioclase, orthopyroxene, and hornblende in MO. The calculation shows the crystallinities of 16 and 45 vol% for MY and MO samples, respectively. These crystallinities represent the averaged values; hence, the crystallinity in each sample used for a deformation experiment may show the variation. However, the chemical composition of groundmass is homogeneous and image analyses for the MO sample show the crystallinity of 47 vol% (see below); we believe that the crystallinities are accurate to ±5 vol%.

For the MO sample, the size distribution of crystals was measured (Fig. 2). To cover the wide range of size, we obtained images under an optical microscope and backscattered electron (BSE) images by using a scanning electron microscope, and manually traced the outlines of crystals (Fig. 2a and b). The numbers and shapes of crystals were determined using image processing software (ImageJ). The size distribution of crystals obtained from two-dimensional images was converted to that in three dimensions using CSD corrections (Higgins, 2000). For the conversion, we used the crystal shape (short–intermediate–long axis) of 1:1.2:9 and 1:2:7 for optical microscopic images and BSE images, respectively, which were obtained by CSDslice5 (Morgan and Jerram, 2006). In the optical microscopic images, the crystals >500 μm show the shape of 1:1.8:2.7, although the average shape for all the

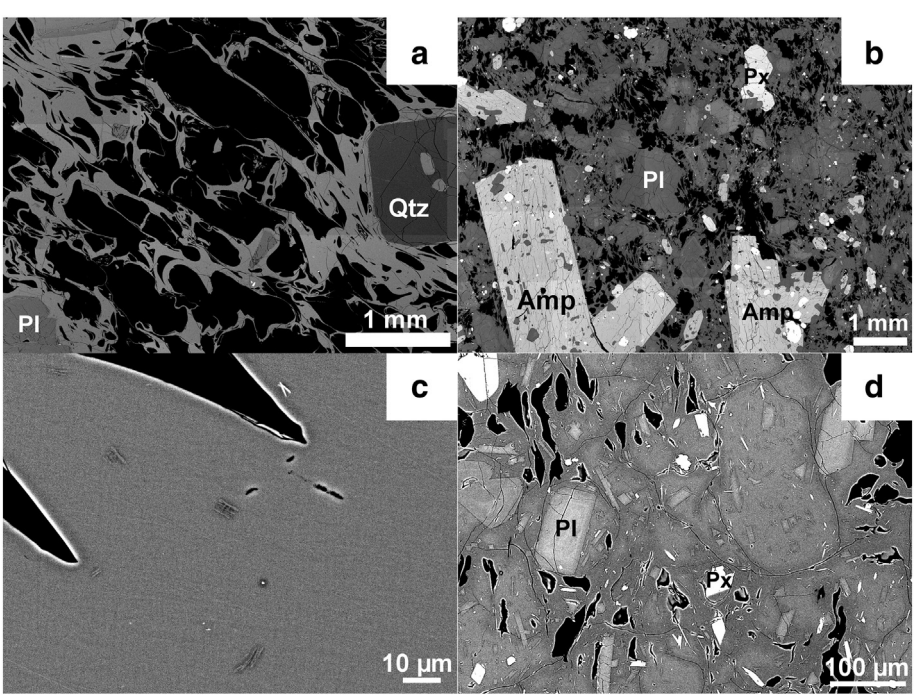

Fig. 1. Backscattered electron images of samples from (a), (c) lava of Mukaiyama volcano, Niijima, Japan (MY) and (b), (d) pumice of the Ootagirigawa pyroclastic flow, Myoko volcano, Japan (MO). Mineral phases of Qtz, Pl, Px, and Amp represent quartz, plagioclase, pyroxene, and amphibole, respectively. In the MY sample, the crystal size is almost unimodal, and the groundmass is glassy. In contrast, the MO sample shows microlites in the groundmass and crystals with a wide range in size.

Table 1
Chemical composition of starting materials.

	MY		MO	
(wt%)	Glass	Bulk	Glass	Bulk
SiO_2	77.5	77.0	76.9	64.2
TiO_2	0.1	0.1	0.2	0.5
Al_2O_3	12.6	12.8	12.1	16.4
FeO	0.7	0.9	1.0	5.3
MnO	0.1	0.1	0.0	0.1
MgO	0.1	0.2	0.1	2.2
CaO	0.5	0.9	1.1	5.7
Na_2O	4.4	4.8	3.1	2.8
K_2O	3.6	2.9	4.7	2.3
P_2O_5	0.0	0.0	0.0	0.1
H_2O	0.4	0.3	0.8	0.4
Total[a]	100.0	100.0	100.0	100.0
η_{melt} at 800 °C[b]	1.3×10^9	–	3.1×10^8	–
Crystal (vol%)	16		45	

[a] The anhydrous composition was normalized to (100 - H_2O).
[b] Melt viscosity at a temperature of 800 °C, estimated based on Giordano et al. (2008).

crystals is 1:1.2:9. This means that large phenocrysts have relatively subrounded shape but small crystals are strongly elongated, which are originated from phenocryst breakage and formation of microlite. The size distribution of crystals shows three straight lines in the CSD plot (Fig. 2c). A steep line represents the CSD of microlites. Moreover, two additional straight lines may reflect phenocrysts with different size ranges, although the difference in the gradient of those lines is small. The crystallinities obtained from image analyses are 35.8 and 10.9 vol% for phenocryst and microlite, respectively; a total crystallinity of 46.7 vol% is consistent with that from mass balance calculation. For the MY sample, the range of crystal size is clearly narrow (Fig. 1a), and it was difficult to measure a representative number of crystal owing to low number densities.

The bulk water content was measured to be 0.3 and 0.4 wt% for MY and MO, respectively, by Karl Fischer titration (KFT) (Table 1). For its determination, we used a stepwise heating technique and considered that water released above 400 °C represents magmatic water (e.g., DeGroat-Nelson et al., 2001; Giachetti and Gonnermann, 2013). When we simply recalculate the water content in matrix glass by using crystal content, the water content is 0.4 and 0.8 wt% for MY and MO samples, respectively. For the MO sample, the contribution of hornblende is <0.1 wt% water because its mode is ~4 wt%, based on mass balance calculation. For the MY sample, the effect of the trace amount of biotite can be ignored. By considering other sources for the uncertainty of the KFT analysis (e.g., Behrens, 1995; Okumura et al., 2003), water contents reported have the error of 0.1 wt%.

The cylindrical samples used for the deformation experiments were cored from sample blocks and their sizes were 15 mm in diameter and 13.6–16.2 mm in length. The total porosity of the samples was measured by X-ray computed tomography (CT) according to the method of Okumura and Sasaki (2014) (Fig. 3 and Table 2). The MY and MO porosities were measured to be 17.5–22.0 and 19.9–24.7 vol%, respectively. The porosities measured by X-ray CT are consistent with those calculated from the bulk density measured by the glass bead method (Sasaki and Katsui, 1981), with the assumption of solid phase densities of 2100 and 2300 kg m^{-3} for MY and MO samples, respectively.

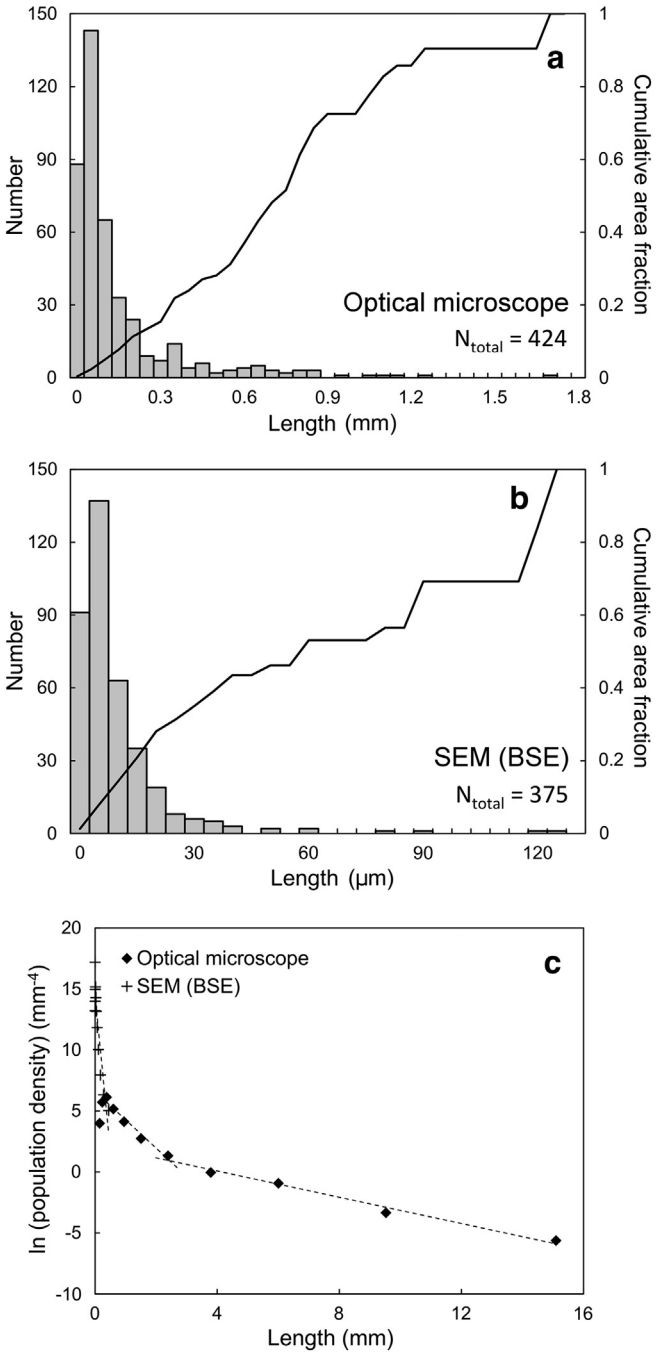

Fig. 2. Crystal size distribution (CSD) of the pumice (MO). (a) The number and cumulative area of crystals counted from images which were obtained from a thin section under an optical microscope. The length was measured for the major axis of an ellipse fitted to a crystal. (b) The number and cumulative area of crystals obtained from backscattered electron images. (c) CSD in three dimensions. The CSD can be explained by the following three straight lines: $\ln n = -0.5386\,L + 2.2385$ ($R^2 = 0.9843$), $\ln n = -2.3293\,L + 6.6088$ ($R^2 = 0.9697$), and $\ln n = -25.475\,L + 14.474$ ($R^2 = 0.8537$), where n and L represent the population density and length of crystal, respectively.

2.2. Heating and deformation experiments

The heating and deformation experiments were performed at a temperature of 800 °C under a pressure of 100 MPa using an internally heated gas-medium deformation apparatus at ISTO, Université d'Orléans (Paterson deformation apparatus, Australian Scientific Instruments Pty Ltd., Paterson and Olgaard, 2000), following the procedure outlined by Champallier et al. (2008). In this study, we controlled both pore pressure and confining pressure during deformation. The effective pressure on the sample (the difference between pore pressure and confining pressure) was kept constant at ~20 MPa during deformation.

Before proceeding with the deformation experiments, we performed heating experiments to check the initial, undeformed microstructure of the samples under high temperature and pressure. The samples were sandwiched between permeable alumina and partially stabilised zirconia spacers and each assembly was enclosed in an iron jacket with a thickness of 0.2 mm. Each assembly was placed in the Paterson deformation apparatus and heated to 800 °C under a confining

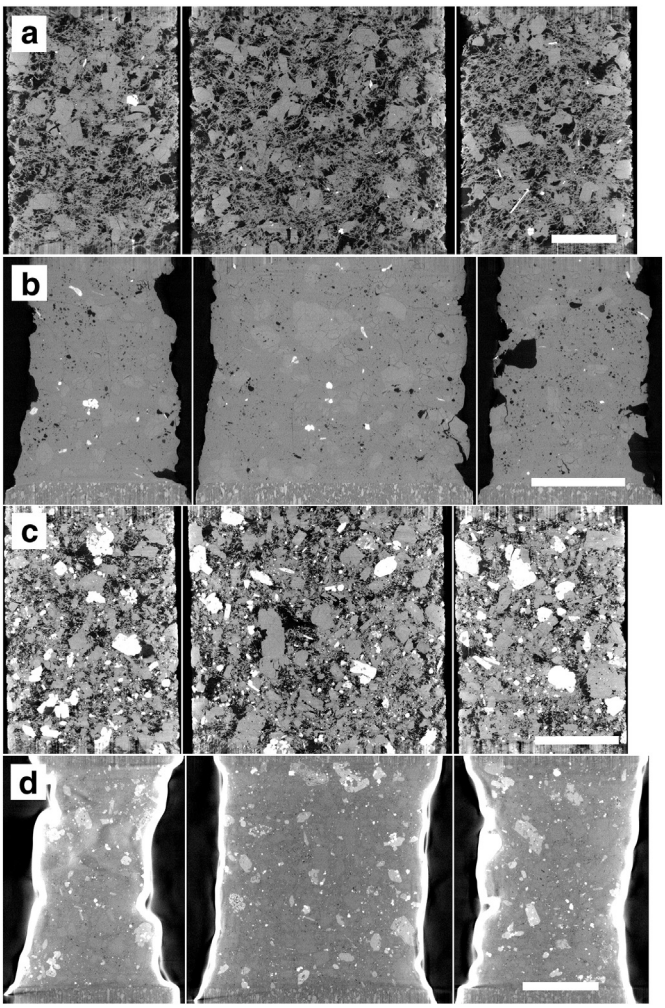

Fig. 3. Vertical slice images of (a), (c) starting columnar samples and (b), (d) run products after the heating experiment (PP400 and PP486) obtained by X-ray CT. (a), (b) and (c), (d) images represent the MY and MO samples, respectively. The centre images represent the longitudinal axis images of columnar samples, and the right and left images correspond to longitudinal tangential sections (Paterson and Olgaard, 2000). In (d), an iron jacket (white area on the sample) surrounds the run product, and porous alumina spacers are found at the top and bottom. The fraction of pores (black portions in the sample) was high before heating experiments, although it strongly decreased after heating and deformation. The white scale bar is 5 mm long.

pressure of 100 MPa (20 MPa effective pressure). Under these conditions, the sample was allowed to dwell for ~1 h. The temperature across the sample did not vary by >2 °C. After 1 h the sample was isobarically quenched to preserve its microstructure, which was investigated by X-ray CT (Fig. 3). Two important observations made from these experiments are that the total porosity of the magmas strongly decreased and the bubble shapes became spherical. If we simply assume that the relaxation timescale of bubble shape can be estimated by the relation of $r\eta/\sigma$, where r, η, and σ represent bubble radius, melt viscosity, and surface tension, respectively (e.g., Navon and Lyakhovsky, 1998), the estimated timescale is roughly comparable with ~1 h, assuming bubble radii of 1–10 μm and a surface tension of 0.32 N m (Bagdassarov et al., 2000). At 800 °C, the melt viscosities are estimated to be 1.3×10^9 (MY) and 3.1×10^8 (MO) Pa s according to the melt composition based on the model of Giordano et al. (2008) (Table 2). Sample dehydration during heating is negligible for deformation experiments, because diffusion distance of water (~60 μm), estimated based on the relation of $(Dt)^{1/2}$, where D and t represent water diffusivity and time, and water diffusivity of 1 $\mu m^2\ s^{-1}$ at a temperature of 800 °C (Zhang, 1999a, 1999b), is much shorter than sample size (15 mm in diameter).

For the deformation experiments, we prepared sample assemblies as described above for the heating experiments. After setting the assembly in the Paterson deformation apparatus, we increased the confining and pore pressures to ~100 and ~80 MPa, respectively; then, the temperature was increased to 800 °C. The sample was allowed to stabilise under these conditions for 1 h. Both the confining medium and pore fluid were argon. Torsional deformation was applied by an external motor, and the torque was measured by an internal load cell. The twisting rates used in this study are 126–1903 μrad s^{-1}, corresponding to strain rates of 6×10^{-5}–$1 \times 10^{-3}\ s^{-1}$ at the outermost part of samples. Under these experimental conditions, the capillary number is calculated to be 2.4–40 for MY and 0.6–9.7 for MO when the bubble radius is assumed to be 10 μm. The mechanical data were corrected for the strength of the iron jacket according to the deformation laws for iron (Frost and Ashby, 1982).

We performed five deformation experiments including four strain rate stepping experiments, in which the strain rate was increased in stepwise increments (e.g., Caricchi et al., 2007; Champallier et al., 2008) (Fig. 4 and Table 2). After deformation, the samples were isobarically quenched, and the microstructure of the run products was analysed by X-ray CT. The X-ray CT analyses were performed for all run products with iron jackets and for selected run products after the iron jacket was removed (PP485 and PP487). Some of the run products show sample-scale fractures and crystal fragmentation, as described in the following section. The porosity of the run products without the jacket was determined to be 1–4 vol% (Table 2).

3. Experimental results

All mechanical data obtained in this study are shown in Fig. 4 and are summarised in Table 2. On the basis of these data, we calculated the magma viscosity under the experimental conditions and compared the results with those of previous studies. The analytical methods of the mechanical data, calculated viscosity, and microstructure of the run products are shown below.

3.1. Mechanical data

3.1.1. Analyses of data

We calculated the bulk viscosity of the magma by essentially following the method of Champallier et al. (2008). However, we checked the effect of yield stress on magma rheology, which was not considered in the previous study.

We assumed that the viscosity of the crystal-bearing magma has yield stress when the crystallinity is larger than a critical value (e.g., Lejeune and Richet, 1995). Then, the rheology of the crystal-bearing magma can be described by the Herschel-Bulkley model:

$$\tau_r = \tau_0 + K\dot{\gamma}_r{}^n, \tag{1}$$

where τ_r and γ_r represent shear stress and strain rate, and τ_0, K, and n are the yield stress, the consistency, and the flow index, respectively. Most rock deformation tests do not include τ_0 and a simple relationship between τ_r and the torque necessary for twisting a sample, M, can be obtained (Paterson and Olgaard, 2000). We expand this relation to the case of magma that can be approximated by the Herschel-Bulkley model. If we assume that the rheology of the magmas is expressed by Eq. (1), the relationship between τ_r and M is given by the following equation (Appendix):

$$M = \frac{\pi\tau_0 d^3}{12} + \frac{\pi d^3}{4(n+3)}(\tau - \tau_0), \tag{2}$$

Table 2
Summary of experimental results.

		Bulk density[a]	Porosity		Length[d]	Diameter[d]	Twisting rate	Strain rate	Torque	η_{app}[e]	n	K	Comment
		(g cm^{-3})	(vol%)[b]	(vol%)[c]	(mm)	(mm)	(μrad s^{-1})	(s^{-1})	(N m)	(Pa s)		(Pa s^n)	
MY	PP400	1.63	22.0	1.0	16.0	15	–	–	–	–	–	–	Heating
	PP482	1.65	17.5	–	15.7	15	126	6.02×10^{-5}	0.876	2.01×10^{10}	0.83 ± 0.08	4.39×10^{9}	Stepping test &
							209	9.99×10^{-5}	1.459	2.11×10^{10}			Sample-scale fracture
							418	2.00×10^{-4}	2.849	2.06×10^{10}			
							839	4.01×10^{-4}	4.165	1.50×10^{10}			
	PP487	1.57	20.0	4.1	16.1	15	213	9.90×10^{-5}	0.098	1.49×10^{9}	1.00 ± 0.20	2.60×10^{9}	Stepping test
							427	1.99×10^{-4}	0.348	2.65×10^{9}			
							862	4.01×10^{-4}	0.755	2.84×10^{9}			
							218	1.01×10^{-4}	0.288	4.29×10^{9}			
							427	1.99×10^{-4}	0.406	3.09×10^{9}			
							856	3.98×10^{-4}	0.644	2.44×10^{9}			
							1290	6.00×10^{-4}	0.981	2.47×10^{9}			
MO	PP486	1.86	22.3	–	16.2	15	–	–	–	–	–	–	Heating
	PP481	1.81	19.9	–	13.6	15	182	1.00×10^{-4}	0.439	5.41×10^{9}	0.28 ± 0.05	7.04×10^{6}	Stepping test
							546	3.01×10^{-4}	0.636	2.61×10^{9}			
							1092	6.02×10^{-4}	0.712	1.46×10^{9}			
	PP485	1.83	21.3	1.1	14.3	15	194	1.02×10^{-4}	0.756	9.55×10^{9}	0.41 ± 0.03	4.21×10^{7}	Stepping test
							570	2.99×10^{-4}	1.289	5.54×10^{9}			
							1143	6.00×10^{-4}	1.544	3.31×10^{9}			
							1903	9.99×10^{-4}	1.960	2.52×10^{9}			
	PP483	1.81	24.7	–	14.3	15	190	9.99×10^{-5}	0.865	1.09×10^{10}	–	–	Constant rate, $\gamma = 1$
							190	9.99×10^{-5}	4.892	6.15×10^{10}			Sample-scale fracture

[a] Bulk density of sample cores measured by the glass bead method.
[b] Porosity before an experiment, measured by the X-ray CT.
[c] Porosity after the experiment, measured by the X-ray CT.
[d] Length and diameter of sample cores used for heating and deformation experiments.
[e] Apparent viscosity at a specific strain rate. See text for further details.

where d represents the sample diameter, and τ is the shear stress at the outermost part of the sample. Combining Eqs. (1) and (2), we obtain the following equation:

$$M = \frac{\pi\tau_0 d^3}{12} + \frac{\pi d^3}{4(n+3)} K\dot{\gamma}^n, \quad (3)$$

where γ is the strain rate at the outermost part of the sample. Based on Eq. (3), we plotted the experimental data in strain rate–torque space (Fig. 5). When the data are fit to Eq. (3), the best-fit curves have $\tau_0 = 0$, which means that the magmas studied in this study do not show clear yield stress. In this case, the values of n and K can be determined by fitting the data with Eq. (3) (Table 2). When $\tau_0 = 0$, Eq. (2) is identical to Eq. (7) in Champallier et al. (2008).

3.1.2. Flow index and magma viscosity

We summarise the flow index (n) and consistency (K) in Table 2 and also indicate the apparent viscosity which is defined as $\eta_{app} = \tau/\gamma$. The consistency (unit of Pa s^n) corresponds to the Newtonian viscosity only when the fluid is Newtonian ($n = 1$; $\tau_0 = 0$). For fluids without yield stress, the Herschel-Bulkley model (Eq. (1)) becomes to be $\tau = K\gamma^n$; hence, the apparent viscosity can be calculated by the relation of $\eta_{app} = K\gamma^{(n-1)}$. The apparent viscosities calculated at specific strain rates are shown in Table 2.

The flow indices obtained for MY and MO are 0.8–1.0 and 0.3–0.4, respectively. The values of MY ($n = 0.8$–1.0) are similar to those obtained for synthetic magmas with relatively isotropic crystals (Champallier et al., 2008), whereas the indices of MO ($n = 0.3$–0.4) are smaller than those of previous studies (e.g., Champallier et al., 2008; Pistone et al., 2012) (Fig. 6). The MO values are also lower than that estimated from the model with the assumption of $r_p = 1$ and 3, where r_p is the aspect ratio of crystal (Mader et al., 2013). In contrast, the flow indices obtained from natural samples (Avard and Whittington, 2012; Vona et al., 2013) are consistent with the MO values, although the effect of crystal shape and size and experimental condition need to be considered. As clearly shown in Fig. 7, the flow index represents the dependence of the viscosity on the strain rate. A detailed comparison of these data and previous studies is given in the following section.

Our viscosity data indicate large variation even when the same sample was used as a starting material. For example, the viscosity of the MY sample (PP482 and PP487) shows a difference of one order of magnitude. The MO (PP481 and PP485) sample also indicates the variation of ~0.3 log units. In addition, in the experiment showing strain hardening (PP483; Fig. 4), the magma viscosity is one order of magnitude larger than those obtained from other experiments (PP481 and PP485). These variations appear to be explained by crystal interaction, which obstructs magma deformation because all samples that showed large viscosity include sample-scale fracturing, as discussed further in the following section.

3.2. Microstructure of run products

Typical tomography slice images of run products are shown in Fig. 8. The samples used here have initial porosities of 18–25 vol%; the porosities decreased to 1–4 vol% after heating and deformation (Table 2). It should be noted that the reduction of the porosity was caused by heating and pressurization, as shown by heating experiments.

Sample-scale fractures are found in high viscosity samples (Fig. 8a and c), whereas less-viscous samples do not include such fractures (Fig. 8b and d). Large phenocrysts along the fractures are fragmented into small pieces, although the fragments are arranged in a jigsaw pattern with no clear indication of movement (Fig. 9). This suggests that the magma stiffened locally, likely due to crystal interaction, resulting in the obstruction of deformation and the formation of sample-scale fracturing. An important point is that the crystal interaction increased the bulk viscosity, eventually leading to sample embrittlement and

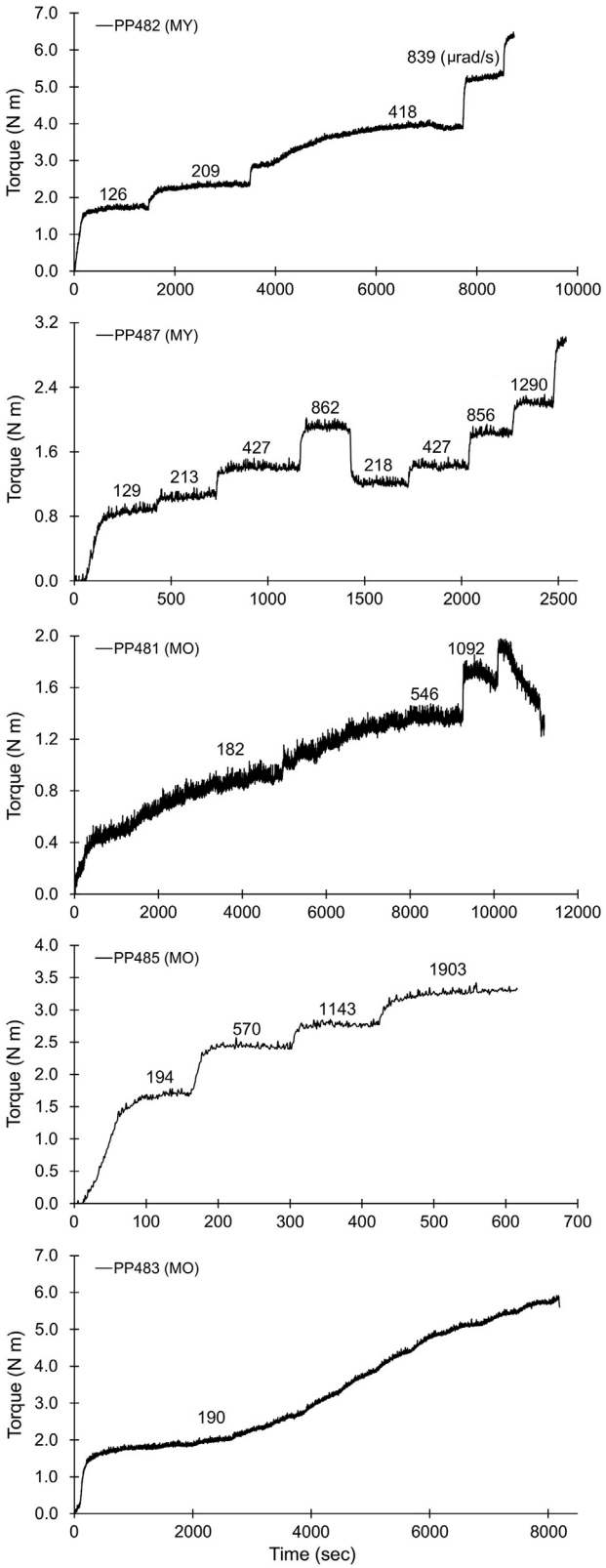

Fig. 4. Torque measured by an internal load cell during sample deformation. The numbers represent twisting rates (μrad s^{-1}). In the PP481 experiment, the sample was fractured just after changing the twisting rate from 1092 to 1819 μrad s^{-1}. In the PP 483 experiment, strain hardening was found, and two torques, i.e. first stable value around 2000 s and final maximum value, were used to calculate viscosity.

fracturing. The relatively stiff part in samples could not be deformed; thus, the deformation rate locally increased in weaker parts that showed viscous deformation. In contrast, the fracturing of synthetic

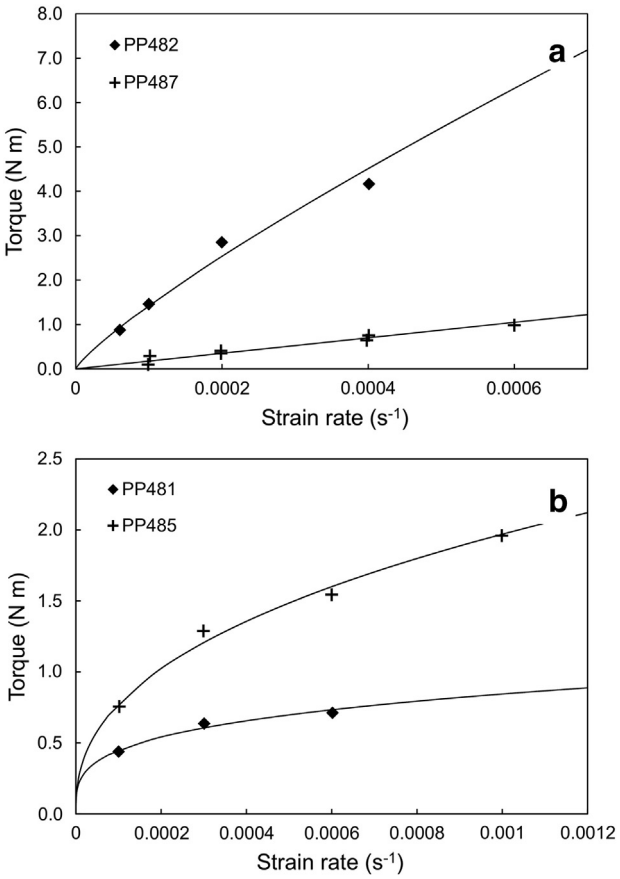

Fig. 5. Relationship between strain rate and torque for samples of (a) MY (16 vol% crystallinity) and (b) MO (45 vol%). Solid curves represent best-fit results by Eq.(3).

magmas was also reported to cause stress drop during torsional deformation (Cordonnier et al., 2012; Pistone et al., 2016). The difference between this study and previous studies seems to be originated by the heterogeneity of the strength in a sample, which would be induced by the combination of different sizes and shapes of crystals and heterogeneous distribution of the crystals. In synthetic magmas, the strength is

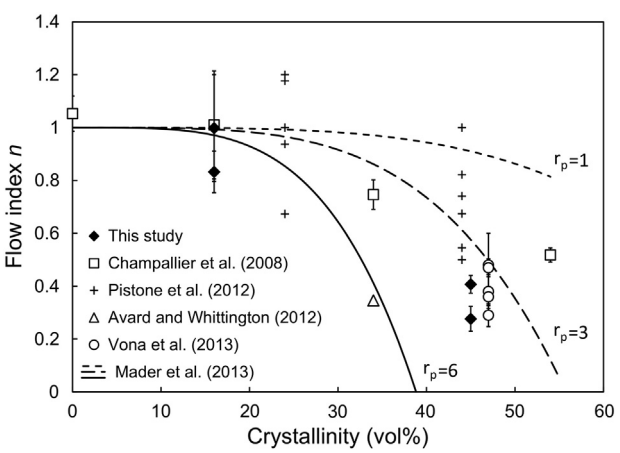

Fig. 6. Flow index (n) plotted as a function of crystallinity. For comparison, the flow indices obtained for synthetic magma analogue with crystals (Champallier et al., 2008), synthetic crystalline magma with gas bubbles (Pistone et al., 2012), and natural rocks (Avard and Whittington, 2012; Vona et al., 2013) are shown, together with the values estimated by the model (Mader et al., 2013). In the model estimate, the shape of crystal (r_p) is assumed to be 1, 3, and 6. At low crystallinity, the experimental data show good agreement with the model, whereas the variation of data increases at high crystallinity. In particular, our data are lower than those predicted by the model.

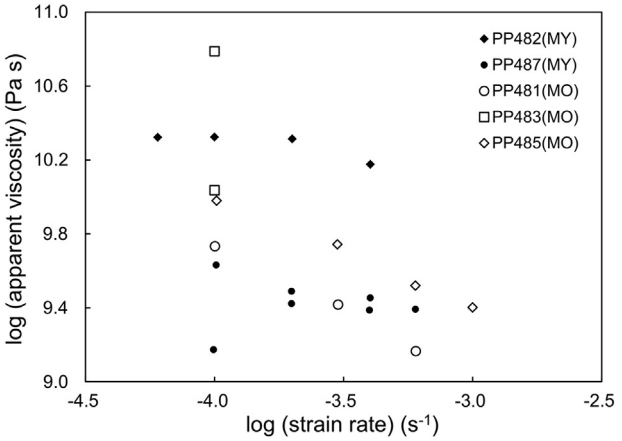

Fig. 7. Dependence of apparent viscosity on strain rate. The low crystallinity sample (MY) shows no clear dependence on the strain rate, whereas the viscosity decreases with the strain rate at high crystallinity (MO). Even with the same sample, the viscosity shows large variation when a crystal network is locally formed.

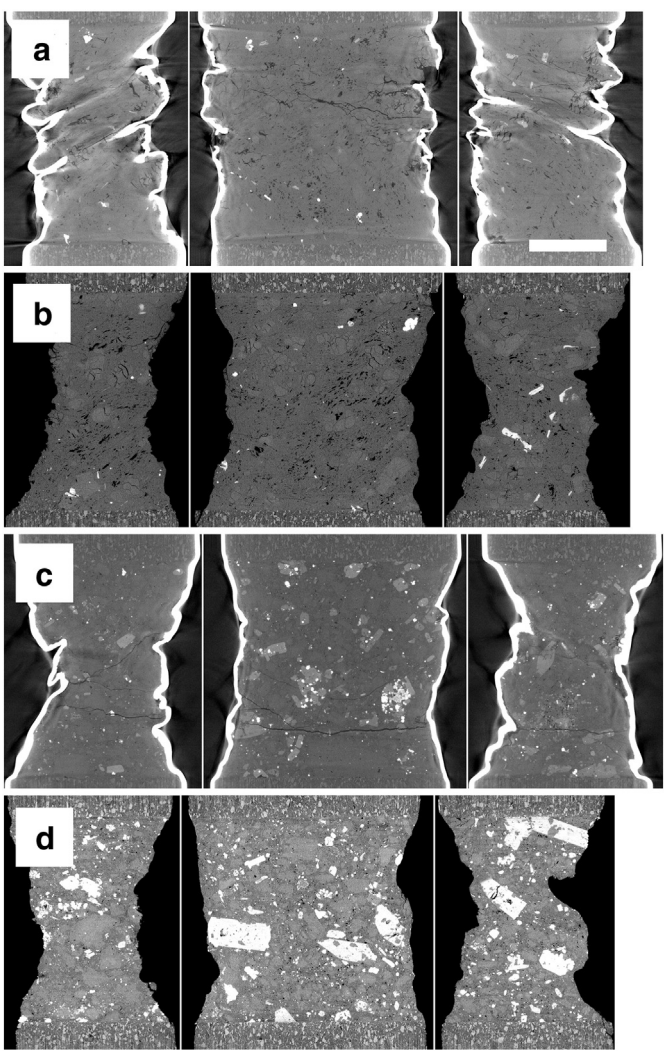

Fig. 8. Vertical slice images of deformed samples obtained by X-ray CT. (a) PP482 and (b) PP487 from MY sample (16 vol% crystallinity). (c) PP483 and (d) PP485 from MO sample (45 vol%). The centre images represent longitudinal axis images, and the right and left images are longitudinal tangential sections. In (a) and (c), sample-scale fractures were found, whereas such fractures were not observed in (b) and (d). The white scale bar is 5 mm long.

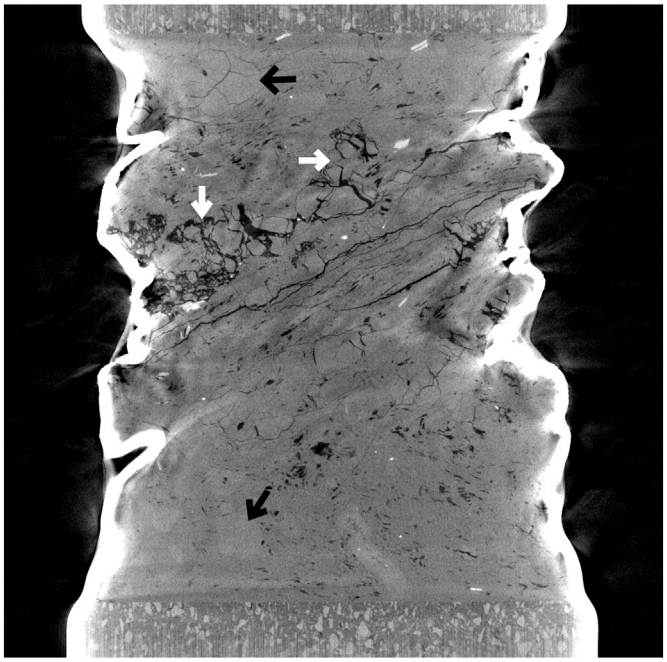

Fig. 9. Vertical slice images of PP482 obtained by X-ray CT. The fragmented phenocrysts of plagioclase along fractures (white arrows) are arranged in a jigsaw pattern. No clear fragmentation is observed for phenocrysts which are not situated along the fractures (black arrows). The width of the image is 16.64 mm.

relatively homogeneous; hence, the deformation localises in the fracture zone once a sample is broken.

4. Discussion

4.1. Comparison with previous studies

Our data indicate that magma viscosity depends on crystallinity and shear strain rate. The flow index reflects the dependence of magma viscosity on shear strain rate. Previous experiments demonstrated that the flow index depends on crystallinity and rapidly decreases near the maximum packing fraction of the crystals (e.g., Champallier et al., 2008; Mueller et al., 2010). The flow index also decreases when crystal aspect ratio is high (Mueller et al., 2010). The physical origin of the reduction of flow index (shear thinning behavior) is still controversial, but shear heating (Mueller et al., 2010) and preferred alignment of crystals (Ishibashi and Sato, 2007) may contribute to shear thinning behavior.

The flow index obtained at a crystallinity of 16 vol% (MY sample) is perfectly consistent with previous data from bubble-free magma and model prediction (Fig. 6). Although it has been reported that gas bubbles of ~10 vol% can cause shear thickening at low crystallinity under shear flow with capillary numbers similar to those in this study (Pistone et al., 2012), our data indicates no shear thickening or shear thinning. This means that only 1–4 vol% gas bubbles do not induce detectable non-Newtonian behavior.

The flow index obtained at a crystallinity of 45 vol% (MO sample) is smaller than the value estimated from the model. At crystallinity, the flow index is estimated to be 0.9, based on the maximum packing particle fraction of ~0.55 when we assume crystals with isotropic shapes (Mader et al., 2013). Although the bubble- and crystal-bearing magma show flow indices smaller than those of the model of bubble-free magma (Pistone et al., 2012; Truby et al., 2015), our flow indices are too low to be explained by the gas bubbles. In contrast, the flow indices obtained from natural magmas (Avard and Whittington, 2012; Vona et al., 2013) are similar to that of this study. The magma used by Vona et al. (2013) includes only anisotropic crystals (alkaline feldspar) (aspect ratio of 1:10); the low flow index seems to be explained by the effect

of crystal shape. The samples used by Avard and Whittington (2012) were dacitic lavas from Santiaguito volcano, Guatemala, which include 30 vol% phenocrysts, 4 vol% microlites, and 11 vol% pore space. This is similar to the MO sample; the magma also show lower flow index than model prediction (Fig. 6). A possible explanation for the small flow index is that the sample contains crystals with different sizes and shapes (Fig. 2). Recent analogue experiments (Cimarelli et al., 2011; Moitra and Gonnermann, 2015) have demonstrated that the combination of different crystal size and shape causes complicated rheology and that the flow index strongly decreases when small anisotropic particles are included into the mixture of fluid and large spherical particles. The crystal habit (short–intermediate–long axis) for MO is 1:1.8:2.7 for crystals >500 μm, 1:1.2:9 for those <300 μm (Fig. 2a), and 1:2:6 for those obtained from BSE images (Fig. 2b). This means that the studied magma includes relatively isotropic large crystals (phenocryst) and acicular small crystals (microlite). Therefore, natural magmas with a wide range of crystal sizes and shapes can have stronger dependence of viscosity on the strain rate than synthetic magma analogue including crystals with similar sizes and shapes.

We show the dependence of magma viscosity (relative viscosity of bulk magma viscosity to melt viscosity) on crystallinity in Fig. 10. The melt viscosity is estimated based on the model of Giordano et al. (2008); the uncertainty of melt viscosity, which originates from the error of water content analysis (±0.1 wt%), yields the errors on the relative viscosity. The viscosity of magma with 16 vol% crystallinity (MY) is consistent with that calculated from Newtonian models (Mader et al., 2013) when the sample does not include the effect of a strong crystal network (PP482). The viscosity of the MO sample with 45 vol% crystallinity is slightly lower than the value predicted by the model (even if $r_p = 1$) when sample-scale fractures were not found. This could result from the combination of different sizes and shapes of crystals.

4.2. Implication for the ascent of crystalline magma in a volcanic conduit

Our experiments using natural magmas showed that magma rheology is accurately predicted by rheological models at low crystallinity (16 vol%), though the variation in crystal size and shape should be considered at high crystallinity (45 vol%). In particular, the flow index obtained at high crystallinity is much smaller than that predicted by existing models. On the basis of these results, we discuss the ascent processes of highly crystalline magma, i.e. ~45 vol% crystallinity.

Magma ascending in a volcanic conduit experiences shear deformation. Shear-induced bubble coalescence and magma fracturing increases the gas permeability of the magma, resulting in outgassing (e.g., Okumura et al., 2008, 2009, 2010). In fact, natural rocks that experienced deformation and outgassing show high gas permeability even at low porosity (e.g., Saar and Manga, 1999; Mueller et al., 2005), as demonstrated by porosity reduction by heating experiments of this study, whereas high gas permeability cannot be reproduced by decompression experiments under isotropic condition (Takeuchi et al., 2009; Lindoo et al., 2016). The outgassing also changes the magma rheology via the decrease in bubble content (e.g., Caricchi et al., 2011; Laumonier et al., 2011). Hence, outgassing and magma rheology play into a feedback loop throughout magma ascent and eruption. When magma with high crystallinity ascends in the conduit, magma deformation is expected to localise near the conduit rim because magma has small flow index, and the strain rate is high at the rim. Hence, magma has relatively low viscosity at the rim (Moitra and Gonnermann, 2015). This localisation inhibits deformation of the magma in the central portion of the conduit, which means that the flow of magma with high crystallinity in the conduit is likely plug-type. However, this scenario is problematic for the formation of dense, crystal-rich magma such as that observed at the 1995–1999 eruption of the Soufrière volcano (Devine et al., 1998) and the 2004–2006 eruption of Mt. St. Helens (Cashman et al., 2008) because outgassing from crystal-rich magma appears to be difficult without shear deformation and fracturing (Laumonier et al., 2011; Okumura et al., 2012; Shields et al., 2014). A possible explanation may be the repetition of shear localisation and outgassing. Near the conduit rim, where shear localises, magma experiences efficient outgassing via shear-induced gas bubble segregation and fracturing (Laumonier et al., 2011; Shields et al., 2014). Once the vesicularity decreases by annealing and compaction, the lateral variation of the viscosity changes, and shear may begin to localise to other regions of the conduit. By repeating this process, densification may occur in crystal-rich magma. This process has been confirmed in crystal-poor magma (e.g., Tuffen and Dingwell, 2005), although no clear evidence has been reported in crystal-rich magma. Hence, additional studies are needed to clarify the mechanism of outgassing from crystal-rich magma.

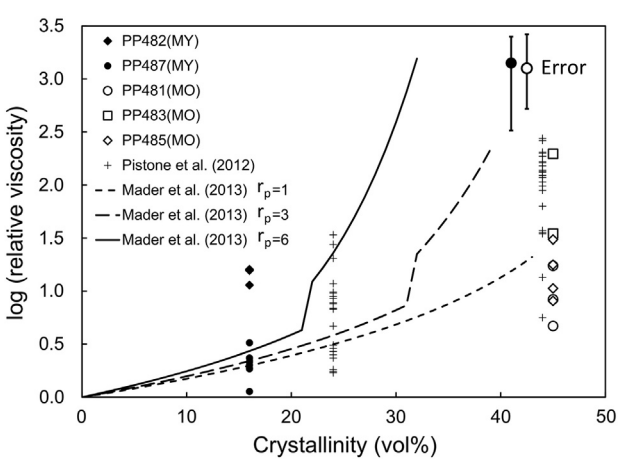

Fig. 10. Dependence of relative viscosity (the ratio of bulk apparent viscosity to melt viscosity) on crystallinity. For comparison, the relative viscosities of bubble-bearing crystalline magma (Pistone et al., 2012) are shown, together with the values estimated by the model, assuming the strain rate of 10^{-4} s^{-1} (Mader et al., 2013). The discontinuities found in the model curves ($r_p = 3$ and 6) are artificially originated due to the transition from Newtonian to non-Newtonian behavior (Mader et al., 2013). The solid and open circles with error bars in the upper right corner represent typical error for MY and MO samples. The error is derived from the uncertainty of water content analysis (±0.1 wt%).

5. Conclusions

We investigated the rheology of two natural magmas with different crystal and bubble shapes and sizes, by performing torsional deformation experiments at 800 °C and 100 MPa (effective pressure of 20 MPa). The viscosities of the magma were determined for strain rates of 6×10^{-5}–1×10^{-3} s^{-1}. The viscosity of magma with a crystallinity of 16 vol% shows good agreement with previous data and models. The range of the measured viscosity of samples at high crystallinity (45 vol%) is slightly lower than those of previous studies and models; the flow index obtained at 45 vol% crystallinity is much smaller than those determined by previous studies using synthetic magma analogue. This may be explained by considering the effect of different sizes and shapes of crystals on the flow index. We also observed that the locally stiff regions were created in the magma, resulting in the formation of sample-scale fractures and increase in the magma viscosity. As was expected on the basis of the previous data, crystal-rich magma appears to experience shear localisation when it ascends in a volcanic conduit because the viscosity of the magma decreases near the conduit rim. This results in plug-type magma flow, resulting in the inhibition of shear-induced outgassing in the central portion of the conduit. Therefore, we may need to consider an unrecognised mechanism for outgassing and the formation of dense crystal-rich magma.

Acknowledgments

This study was carried out during the visit of SO to the deformation laboratory of ISTO, University of Orleans, and supported by the Leading Young Researcher Overseas Visit Program of Tohoku University and Grants-in-aid for Scientific Research in Japan (No. 15H03714). Funding for ARLK was provided by a Postgraduate Scholarship-Doctoral (CGS D3) provided by the Natural Sciences and Engineering Research Council of Canada (NSERC) (number CGSD3-444207-2013). Constructive comments by Alessandro Vona and an anonymous reviewer improved the manuscript.

Appendix A. Appendix

We analysed the relationship between torque and strain rate during torsional deformation of a columnar sample, following the procedure of Paterson and Olgaard (2000). We assumed that the sample is approximated by the Herschel-Bulkley model:

$$\tau_r = \tau_0 + K_r \dot{\gamma}_r{}^n, \tag{A1}$$

where τ_r and γ_r represent shear stress and strain rate, and τ_0, K_r, and n are the yield stress, the consistency and the flow index, respectively. At the outermost edge of the sample, the relation is given by the following equation:

$$\tau = \tau_0 + K\dot{\gamma}^n, \tag{A2}$$

Here, we simply assumed that K_r/K is equal to unity, and we used the relationship between strain rate and twisting rate, i.e. $\gamma_r = r\theta/l$ and $\gamma = d\theta/2l$, where r, d, θ, and l represent the radial position in a columnar sample, sample diameter, twisting rate, and sample length, respectively (Paterson and Olgaard, 2000). Then, we obtained the following equation by combining Eqs. (A1) and (A2):

$$\tau_r = \tau_0 + (\tau - \tau_0)\left(\frac{2r}{d}\right)^n. \tag{A3}$$

The torque necessary for twisting the sample is given by integrating shear stress:

$$M = 2\pi\int_0^{d/2}\tau_r r^2 dr. \tag{A4}$$

From Eqs. (A3) and (A4), we obtained the relationship between torque and shear stress as follows:

$$M = \frac{\pi\tau_0 d^3}{12} + \frac{\pi d^3}{4(n+3)}(\tau - \tau_0). \tag{A5}$$

This equation can be changed to the following equation by using Eq. (A2):

$$M = \frac{\pi\tau_0 d^3}{12} + \frac{\pi d^3}{4(n+3)}K\dot{\gamma}^n. \tag{A6}$$

According to Eq. (A6), we can determine the values of τ_0 and n, and K is determined on the basis of Eq. (A2).

It should be noted that in Eq. (A3), the viscosity is assumed to be independent of the radial position in a cylindrical sample, although the viscosity of magma often shows shear thinning or shear thickening effects. Hence, the viscosity depends on the radial position in the sample. Eqs. (A5) and (A6) can be used as good approximations for determining n and K_r because a large proportion of the measured torque relates to an outer fraction of the sample according to Eq. (A4) (Paterson and Olgaard, 2000).

References

Avard, G., Whittington, A.G., 2012. Rheology of arc dacite lavas: experimental determination at low strain rates. Bull. Volcanol. 74, 1039–1056.
Bagdassarov, N., Dorfman, A., Dingwell, D.B., 2000. Effect of alkalis, phosphorus, and water on the surface tension of haplogranitic melt. Am. Mineral. 85, 33–40.
Behrens, H., 1995. Determination of water solubilities in high viscosity melts: an experimental study on $NaAlSi_3O_8$ and $KAlSi_3O_8$ melts. Eur. J. Mineral. 7, 905–920.
Caricchi, L., Burlini, L., Ulmer, P., Gerya, T., Vassalli, M., Papale, P., 2007. Non-Newtonian rheology of crystal-bearing magmas and implications for magma ascent dynamics. Earth Planet. Sci. Lett. 264, 402–419.
Caricchi, L., Giordano, D., Burlini, L., Ulmer, P., Romano, C., 2008. Rheological properties of magma from the 1538 eruption of Monte Nuovo (Phlegrean Fields, Italy): an experimental study. Chem. Geol. 256, 158–171.
Caricchi, L., Pommier, A., Pistone, M., Castro, J., Burgisser, A., Perugini, D., 2011. Strain-induced magma degassing: insights from simple-shear experiments on bubble bearing melt. Bull. Volcanol. 73, 1245–1257.
Cashman, K.V., Thornber, C.R., Pallister, J.S., 2008. From dome to dust: shallow crystallization and fragmentation of conduit magma during the 2004–2006 dome extrusion of Mount St. Helens, Washington. A volcano rekindled: the renewed eruption of Mount St. Helens, 2004–2006 edited by David R. Sherrod, William E. Scott, and Peter H. Stauffer. U.S. Geol. Surv. Prof. Pap. 1750, 387–413.
Champallier, R., Bystricky, M., Arbaret, L., 2008. Experimental investigation of magma rheology at 300 MPa: from pure hydrous melt to 76 vol.% of crystals. Earth Planet. Sci. Lett. 267:571–583. http://dx.doi.org/10.1016/j.epsl.2007.11.065.
Cimarelli, C., Costa, A., Mueller, S., Mader, H.M., 2011. Rheology of magmas with bimodal crystal size and shape distributions: insights from analog experiments. Geochem. Geophys. Geosyst. 12, Q07024. http://dx.doi.org/10.1029/2011GC003606.
Cordonnier, B., et al., 2012. The viscous-brittle transition of crystal-bearing silicic melt: direct observation of magma rupture and healing. Geology 40, 611–614.
DeGroat-Nelson, P.J., Cameron, B.I., Fink, J.H., Holloway, J.R., 2001. Hydrogen isotope analysis of rehydrated silicic lavas: implications for eruption mechanisms. Earth Planet. Sci. Lett. 185, 331–341.
Devine, J.D., Murphy, M.D., Rutherford, M.J., Barclay, J., Sparks, R.S.J., Carroll, M.R., Yound, S.R., Gardner, J.E., 1998. Petrologic evidence for pre-eruptive pressure-temperature conditions, and recent reheating, of andesitic magma erupting at the Soufriere Hills Volcano, Montserrat, W.I. Geophys. Res. Lett. 25, 3669–3672.
Frost, H.J., Ashby, M.F., 1982. Deformation-mechanism Maps: The Plasticity and Creep of Metals and Ceramics. Pergamon Press, New York, p. 167.
Giachetti, T., Gonnermann, H.M., 2013. Water in volcanic pyroclast: rehydration or incomplete degassing? Earth Planet. Sci. Lett. 369–370, 317–332.
Giordano, D., Russell, J.K., Dingwell, D.B., 2008. Viscosity of magmatic liquids: a model. Earth Planet. Sci. Lett. 271, 123–134.
Hasenaka, T., Yoshida, T., Hayatsu, K., 1995. Chemical compositions of lavas from Myoko volcano group. Res. Rep. Lab. Nucl. Sci. 28, 43–82 (in Japanese).
Higgins, M.D., 2000. Measurement of crystal size distribution. Am. Mineral. 85, 1105–1116.
Ishibashi, H., Sato, H., 2007. Viscosity measurements of subliquidus magmas: alkali olivine basalt from the Higashi-Matsuura district, Southwest Japan. J. Volcanol. Geotherm. Res. 160, 223–238.
Isshiki, N., 1987. Geology of the Niijima district. Geol. Surv. Jpn 85 (in Japanese with English abstract).
Kozono, T., Koyaguchi, T., 2012. Effects of gas escape and crystallization on the complexity of conduit flow dynamics during lava dome eruptions. J. Geophys. Res. 117, B08204. http://dx.doi.org/10.1029/2012JB009343.
Laumonier, M., Arbaret, L., Burgisser, A., Champallier, R., 2011. Porosity redistribution enhanced by strain localization in crystal-rich magmas. Geology 39:715–718. http://dx.doi.org/10.1130/G31803.1.
Lavallée, Y., Hess, K.-U., Cordonnier, B., Dingwell, D.B., 2007. Non-Newtonian rheological law for highly crystalline dome lavas. Geology 35:843–846. http://dx.doi.org/10.1130/G23594A.1.
Lejeune, A.-M., Richet, P., 1995. Rheology of crystal-bearing silicate melts: an experimental study at high viscosities. J. Geophys. Res. 100, 4215–4229.
Lindoo, A., Larsen, J.F., Cashman, K.V., Dunn, A.L., Neill, O.K., 2016. An experimental study of permeability development as a function of crystal-free melt viscosity. Earth Planet. Sci. Lett. 435, 45–54.
Llewellin, E.W., Manga, M., 2005. Bubble suspension rheology and implications for conduit flow. J. Volcanol. Geotherm. Res. 143, 205–217.
Llewellin, E.W., Mader, H.M., Wilson, S.D.R., 2002. The rheology of a bubbly liquid. Proceedings of the Royal Society of London. Series A 458, 987–1016.
Mader, H.M., Llewellin, E.W., Mueller, S.P., 2013. The rheology of two-phase magmas: a review and analysis. J. Volcanol. Geotherm. Res. 257:135–158. http://dx.doi.org/10.1016/j.jvolgeores.2013.02.014.
Manga, M., Castro, J., Cashman, K.V., 1998. Rheology of bubble-bearing magmas. J. Volcanol. Geotherm. Res. 87, 15–28.
Marsh, B., 1981. On the crystallinity, probability of occurrence and rheology of lava and magma. Contrib. Mineral. Petrol. 78, 85–98.
Melnik, O., Sparks, R.S.J., 1999. Nonlinear dynamics of lava dome extrusion. Nature 402, 37–41.
Moitra, P., Gonnermann, H.M., 2015. Effects of crystal shape- and size-modality on magma rheology. Geochem. Geophys. Geosyst. 16:1–26. http://dx.doi.org/10.1002/2014GC005554.
Morgan, D., Jerram, D.A., 2006. On estimating crystal shape for crystal size distribution analysis. J. Volcanol. Geotherm. Res. 154, 1–7.
Mueller, S., Melnik, O., Spieler, O., Scheu, B., Dingwell, D.B., 2005. Permeability and degassing of dome lavas undergoing rapid decompression: an experimental determination. Bull. Volcanol. 67, 526–538.

Mueller, S., Llewellin, E.W., Mader, H.M., 2010. The rheology of suspensions of solid particles. Proceedings of the Royal Society of London. Series A 466:1201–1228. http://dx.doi.org/10.1098/rspa.2009.0445.
Mueller, S., Llewellin, E.W., Mader, H.M., 2011. The effect of particle shape on suspension viscosity and implications for magmatic flows. Geophys. Res. Lett. 38, L13316. http://dx.doi.org/10.1029/2011GL047167.
Navon, O., Lyakhovsky, V., 1998. Vesiculation processes in silicic magmas. Geol. Soc. Lond., Spec. Publ. 145, 27–50.
Okumura, S., Sasaki, O., 2014. Permeability reduction of fractured rhyolite in volcanic conduits and its control on eruption cyclicity. Geology 42:843–846. http://dx.doi.org/10.1130/G35855.1.
Okumura, S., Nakamura, M., Nakashima, S., 2003. Determination of molar absorptivity of IR fundamental OH-stretching vibration in rhyolitic glasses. Am. Mineral. 88, 1657–1662.
Okumura, S., Nakamura, M., Tsuchiyama, A., Nakano, T., Uesugi, K., 2008. Evolution of bubble microstructure in sheared rhyolite: formation of a channel-like bubble network. J. Geophys. Res. 113, B07208.
Okumura, S., Nakamura, M., Takeuchi, S., Tsuchiyama, A., Nakano, T., Uesugi, K., 2009. Magma deformation may induce non-explosive volcanism via degassing through bubble networks. Earth Planet. Sci. Lett. 281, 267–274.
Okumura, S., Nakamura, M., Nakano, T., Uesugi, K., Tsuchiyama, A., 2010. Shear deformation experiments on vesicular rhyolite: implications for brittle fracturing, degassing, and compaction of magmas in volcanic conduits. J. Geophys. Res. 115, B06201. http://dx.doi.org/10.1029/2009JB006904.
Okumura, S., Nakamura, M., Nakano, T., Uesugi, K., Tsuchiyama, A., 2012. Experimental constraints on permeable gas transport in crystalline silicic magmas. Contrib. Mineral. Petrol. 164, 493–504.
Pal, R., 2003. Rheological behaviour of bubble-bearing magmas. Earth Planet. Sci. Lett. 207, 165–179.
Papale, P., 1999. Strain-induced magma fragmentation in explosive eruptions. Nature 397, 425–428.
Paterson, M.S., Olgaard, D.L., 2000. Rock deformation tests to large shear strains in torsion. J. Struct. Geol. 22, 1341–1358.
Picard, D., Arbaret, L., Pichavant, M., Champallier, R., Launeau, P., 2013. The rheological transition in plagioclase-bearing magmas. J. Geophys. Res. 118:1363–1377. http://dx.doi.org/10.1002/jgrb.50091.
Pistone, M., Caricchi, L., Ulmer, P., Burlini, L., Ardia, P., Reusser, E., Marone, F., Arbaret, L., 2012. Deformation experiments of bubble- and crystal-bearing magmas: rheological and microstructural analysis. J. Geophys. Res. 117, B05208. http://dx.doi.org/10.1029/2011JB008986.
Pistone, M., Caricchi, L., Ulmer, P., Reusser, E., Ardia, P., 2013. Rheology of volatile-bearing crystal mushes: mobilization vs. viscous death. Chem. Geol. 345, 16–39.
Pistone, M., Cordonnier, B., Caricchi, L., Ulmer, P., Marone, F., 2016. The viscous to brittle transition in crystal- and bubble-bearing magmas. Front. Earth Sci. 3:71. http://dx.doi.org/10.3389/feart.2015.00071.
Saar, M.O., Manga, M., 1999. Permeability-porosity relationship in vesicular basalts. Geophys. Res. Lett. 26, 111–114.
Sasaki, T., Katsui, Y., 1981. A new technique for measuring density of pumice using glass beads. Bull. Volcanol. Soc. Japan. 26, 117–118 (in Japanese).
Scaillet, B., Holtz, F., Pichavant, M., 1998. Phase equilibrium constraints on the viscosity of silicic magmas. 1. Volcanic-plutonic comparison. J. Geophys. Res. 103, 27257–27266.
Shields, J.K., Mader, H.M., Pistone, M., Caricchi, L., Floess, D., Putlitz, B., 2014. Strain-induced outgassing of three-phase magmas during simple shear. J. Geophys. Res. 119. http://dx.doi.org/10.1002/2014JB011111.
Takeuchi, S., 2004. Precursory dike propagation control of viscous magma eruptions. Geology 32, 1001–1004.
Takeuchi, S., Tomiya, A., Shinohara, H., 2009. Degassing conditions for permeable silicic magmas: implications from decompression experiments with constant rates. Earth Planet. Sci. Lett. 283, 101–110.
Truby, J.M., Mueller, S.P., Llewellin, E.W., Mader, H.M., 2015. The rheology of three-phase suspensions at low bubble capillary number. Proceedings of the Royal Society of London. Series A:471 http://dx.doi.org/10.1098/rspa.2014.0557.
Tuffen, H., Dingwell, D., 2005. Fault textures in volcanic conduits: evidence for seismic trigger mechanisms during silicic eruptions. Bull. Volcanol. 67, 370–387.
Vona, A., Romano, C., Giordano, D., Russell, J.K., 2013. The multiphase rheology of magmas from Monte Nuovo. Chem. Geol. 346, 213–227.
Zhang, Y., 1999a. A criterion for the fragmentation of bubbly magma based on brittle failure theory. Nature 402, 648–659.
Zhang, Y., 1999b. H_2O in rhyolitic glasses and melts: measurement, speciation, solubility, and diffusion. Rev. Geophys. 37, 493–516.